Effect of substrate elasticity on thin film buckle morphologies: A phase diagram

F.-Z. Abbes, C. Coupeau, J. Durinck, M. Talea, Y. Ni, G. Parry

Effect of substrate elasticity on thin film buckle morphologies: a phase diagram

F.-Z. Abbes[d], C. Coupeau[a,c,*], J. Durinck[a], M. Talea[d], Y. Ni[c] and G. Parry[b]

[a]*InstitutPprime, Dpt of Physics and Mechanics of Materials, UPR 3346 CNRS-ENSMA-Université de Poitiers, 86000 Poitiers, France*

[b]*SIMaP, UMR 5266 CNRS, Université de Grenoble-Alpes, Grenoble 38000, France*

[c]*CAS Key Laboratory of Mechanical Behavior and Design of Materials, University of Science and Technology of China, Hefei, Anhui 230026, P. R. China*

[d]*Laboratory of Information Processing, Faculty of Sciences Ben M'sik, Hassan II University of Casablanca, Morocco.*

[*]*Corresponding author : christophe.coupeau@univ-poitiers.fr*

Abstract. Thin films submitted to internal/external stresses are known to undergo buckling over a critical stress level. In the case of a rigid substrate, depending on the stress anisotropy, three elementary buckling structures are expected: straight-sided, bubble or telephone cord buckles. In this context, the effect of the substrate elasticity on the expected buckled morphologies is explored. The post-buckling equilibrium shapes that develop on parallel delaminated stripes of films for a biaxial compressive stress state are studied. Finite elements methods calculations are carried out to simulate the various equilibrium configurations. A morphological map is extracted and plotted as a function of the stress components in the longitudinal (*i.e.* along the stripe direction) and transversal direction (*i.e.* perpendicular to the stripe direction). It is shown that the stability domains of the elementary buckles are shifted down to lower stresses as the substrate stiffness is decreased. In addition, the stability domain of the telephone cord buckles is shown to be enlarged. Finally, an intermediate domain between bubbles and both straight-sided and telephone cord buckles is evidenced on the morphological map. The buckles are in this case characterized by hook-like or bone-like structures. This latter buckling structure has been experimentally observed by atomic force microscopy on nickel/polycarbonate systems.

1. Introduction

Thin films, coatings or even 2D materials are now widely used in a large variety of application domains, ~~such as~~ for instance optical devices or thermal barriers in extreme environments. Thin films are often produced by physical vapor sputtering techniques and may develop high internal stresses, sometimes about a few GPa in compression (see [1] for a review). They may then delaminate resulting in various buckling patterns. Preventing buckling is consequently a key issue in the field of coating technology, since it generally results in the loss of functional properties that were initially conferred to the coated materials. On the other hand, controlling the occurrence of buckling can also be of great interest, an example being the creation of designed-channels at the micro-nanometer scale as shown on carbon [2] or molybdenum disulfide MoS_2 films, for nanofluidic applications [3]. Buckling can also enhance a large variety of functional properties, including catalytic activities induced by MoS_2 buckles [4], hydrophobic behavior induced on buckled graphene [5], antimicrobial activities on graphene oxide [6] or buckled graphitic films with shock absorbing properties [7]. By using analytical or numerical equilibrium solutions of stressed plates in the framework of elasticity, buckles can be seen as a morphological signature of the mechanical properties of the associated thin film, such as Young's modulus, internal stresses or film/substrate adherence. It follows that precise buckle characterization may be a good alternative to nanoindentation techniques in the case of very soft substrates [8]. It is consequently of key importance to identify the parameters controlling the occurrence of any given buckles.

Buckling patterns occurring after interfacial delamination of thin films from their substrates have been widely investigated in the frame of the Föppl -Von Karman theory of plates [9]. Among the large variety of buckling structures, the most common are the straight-sided, bubble and telephone cord buckles [10-23]. The latter are also referred to as worm-like buckles in the literature. It is now well known that the telephone cord and bubble patterns are two

buckling modes of the straight-sided buckle and so, are sometimes referred to as secondary buckling patterns. A map of buckling morphologies has already been established from finite element simulations of thin stressed films [24]. It explains in particular why telephone cords are so often experimentally observed in that they are mainly related to isotropic stress states in the film. It should be noted that this morphological map was carried out assuming that the film was clamped along its delamination edges and an infinitely rigid substrate (*i.e.* including contact between the film and a rigid plane located just underneath the film). Additionally, some effects of substrate elasticity have been characterized [19,20,25,26]. It is thus now well-established that the critical stress for buckling to occur strongly decreases for increasingly soft substrates [8,9,25,26]. As a result, the maximum deflection of the associated straight-sided buckle is increased in turn [26]. More recently, it was shown in the case of a straight-sided buckle how the interface toughness at the crack front is modified by the elastic contrast between the film and its substrate [27], and how the stress field that may develop in the substrate over a large distance influences the buckle interaction [28].

In this context, it is the purpose of this work to investigate through finite element simulations, how the map of the buckled morphologies is modified considering the soft elastic character of the substrate. It must be mentioned that the morphology of the buckles may depend on the interface toughness in the case where buckling-driven delamination occurs [14,15,27]. In our experiments, regions of the thin films are first delaminated from the substrate by application of an external uniaxial compression on the substrate. These delaminated areas take the shape of parallel rectangular stripes (forming perpendicular to the compression axis). It has been experimentally demonstrated in previous studies that the delaminated areas between a film and its substrate do not evolve anymore once created (as the external compression is released) [24,28-30]. For this reason no buckling-driven delamination is considered in the present work, but only buckling on delaminated stripes. The morphologies are thus computed as mechanical

equilibrium states for various levels of biaxial compressive loadings applied to the film. ~~Finally, in contrast to our approach, it is worth mentioning a recent approach using inverse analysis on post-buckled shape of shells to identify the unknown applied loads from given displacements and to reconstruct the deformation of the structure [31,32].~~

2. FEM modeling

The simulations have been carried out using the finite elements method, with the ABAQUS software [31]. The type of elements that have been used for the film and for the substrate, the mesh size and the robustness of the calculation with respect to the elements size, is carried out in the Appendix. The simulation box is presented in Fig. 1. It is a parallelepiped of dimensions L_1, L_2 and H along the (Ox), (Oy) and (Oz) directions, respectively. It is composed of two parts: (1) the film modeled as an elastic plate (*i.e.* a 2D structure in the (Oxy) plane) of thickness h, made of an elastic linear material with Young's modulus E_f and Poisson's ratio ν_f; and (2) the substrate modeled as a parallelepiped (3D structure), made of an elastic linear material with Young's modulus E_s and Poisson's ratio ν_s.

The film is perfectly adherent to the substrate (*i.e.* nodes are shared between the plate and the top surface of the substrate, ensuring continuity of the displacement field), except along a rectangular stripe of width $2b$ and length L_1 (bounded by dashed lines in Fig. 1) for which the film and substrate have distinct nodes. The buckling occurs on this part of the film, further designated in the text as the 'delaminated area'. It is worth noting that the width $2b$ remains constant during buckling of the plate, *i.e.* no crack propagation at the film/substrate interface is considered in this study, as discussed previously. A frictionless rigid contact is chosen between the lower film surface and the upper substrate surface and so, the plate is unilaterally constrained

during buckling. Contact areas may thus develop in the delaminated area between the film and the substrate during the post-critical buckling regime of the film. It is necessary to consider a geometrically non-linear plate model in this problem in order to follow the post-critical buckling equilibrium paths and to deal with the transitions between the different patterns. The geometrical non-linear Green-Lagrange strain tensor is therefore used in the computations. The boundary conditions are taken as:

(1) $u_x = 0$, for the two faces of equation $x = 0$ and $x = L_1$,

(2) $u_y = 0$, for the two faces of equation $y = 0$ and $y = L_2$,

(3) $u_z = 0$, for the bottom face, of equation $z = 0$.

An imperfection is introduced over the delaminated area in order to trigger buckling. This consists of slightly moving the nodes belonging to the delaminated area from the flat configuration along the direction normal to the surface (Oz). This gives a modified initial position but does not induce strains. The amplitude of the imperfection that was considered is very small (b/1000). Three types of imperfections were tested: (a) a straight-sided buckle shape, (b) a straight-sided buckle shape perturbed by bubbles at the top and (c) a straight-sided buckle shape perturbed by a telephone cord-like undulation at the top. After trying those different initial imperfection shapes separately, it turned out that the obtained phase diagram was not modified by the choice of the imperfection type. The simplest one (a) was thus retained with a shape chosen in order to match the well-known 'Euler column' solution $u_z(x,y) = \frac{\delta}{2}\left(1 + \cos \pi \frac{y}{b}\right)$, with $u_z(x,y)$ the out-of-plane displacement of the plate along the z direction [9].

A compressive stress state was induced in the film by a thermal loading, in order to mimic the experimental stress state resulting from deposition processes for instance [1]. In order to do

so, anisotropic thermal expansion properties were assigned to the film, with two coefficients χ_1 and χ_2 respectively in the (Ox) and (Oy) directions. As any displacement of the film normal to its boundaries is prevented, a positive variation of temperature ΔT allows inducing a compressive stress state in the plane adherent part of the film given by:

$$\sigma_{xx}^0 = -\frac{E_f}{1-\nu_f^2}\left(\chi_1 + \nu_f \chi_2\right)\Delta T, \qquad \text{Eq. (1)}$$

$$\sigma_{yy}^0 = -\frac{E_f}{1-\nu_f^2}\left(\chi_2 + \nu_f \chi_1\right)\Delta T, \qquad \text{Eq. (2)}$$

$$\sigma_{xy}^0 = 0. \qquad \text{Eq. (3)}$$

The choice of χ_1 and χ_2 allows thus to choose independently σ_{xx}^0 and σ_{yy}^0. The target temperature variation ΔT (*i.e.* the loading parameter) can be artificially set to 1 for this purpose. A maximum increase of 1% of the target (final) loading was allowed for each increment. Finally, the transition from one buckle morphology to another was determined from the evolution of the out-of-plane displacement of the film.

Different elastic mismatches between the film and its substrate have been investigated and characterized by the Dundurs' parameter α, *i.e.* by the reduced film/substrate elastic moduli mismatch, given by:

$$\alpha = \frac{\bar{E}_f - \bar{E}_s}{\bar{E}_f + \bar{E}_s}, \quad \text{with } \bar{E}_f = \frac{E_f}{1-\nu_f^2} \text{ and } \bar{E}_s = \frac{E_s}{1-\nu_s^2}. \qquad \text{Eq. (4)}$$

Thus, α=-1 corresponds to a rigid substrate and α=+1 to an infinitly compliant (soft) substrate.

The values of E_f, ν_f and ν_s were arbitrarily fixed to 160 GPa, 0.31 and 0.34, respectively. α was consequently tuned in the following by changing the E_s value. Note that, in our case, the film and the substrate Poisson's ratios are close to 1/3, which gives a value of β close to α/4 for any value of E_s, as often discussed in literature (*e.g.* [9,28]). ~~The influence of β was thus not investigated in this study.~~ For most of the calculations, the thickness H of the substrate is fixed to 12 μm, while the thickness h of the film is 50 nm. However, for values of α close to +1 (*i.e.* rigid film on very soft substrate) for which the substrate is deformed deeply, higher values of H were taken (H=100μm has been used for ~~soft substrates~~ α = 0.95 and α = 0.99). For the delaminated area, a width $2b$=6 μm is taken. A value $L_2 = 6b$ is typically taken but has been also fixed larger ($L_2 = 18b$) for very soft substrates to avoid boundary artefacts. It is worth noting that the finite size of the simulation box in the x direction constrains the value of the wavelength λ of periodic patterns. This is why the simulation box has been chosen long enough along the (Ox) direction, in order to minimize this effect (L_1=10b). Tests have been carried out with a longer cell (L_1=15b) for one set of material parameters, showing no significant differences on the morphological map. For the sake of clarity, the different parameters used for the FEM modeling have been summarized in Table 1.

3. Results and discussion

A characteristic morphological map for two similar reduced Young moduli of film and substrate (α=0) is shown in Fig. 2a. The transversal (along (Oy)) and longitudinal (main buckle axis along (Ox)) stresses have been normalized as proposed from a dimensional analysis in [24] by:

$$\beta_t = \frac{\sigma_{yy}^0}{\bar{E}_f}\left(\frac{2b}{h}\right)^2, \quad \text{Eq. (5)}$$

$$\beta_l = \frac{\sigma_{xx}^0}{\bar{E}_f}\left(\frac{2b}{h}\right)^2, \quad \text{Eq. (6)}$$

The first data point on the map (for β_t=8) corresponds to the minimum transversal stress for buckling to occur, below which the plate state (lower left side of the map in Fig. 2a) remains energetically favorable [24]. As observed in the case of a rigid substrate (α=-1) [24], the morphological map exhibits three distinct domains, namely related to straight-sided buckles (SSB) for high β_t values, bubbles (B) for high β_l values, and telephone cord buckles (TC) for high isotropic stress states (see the straight green line in Fig. 2a related to β_t=β_l). The characteristic buckling structures are shown in Fig. 2b, highlighted here by the out-of-plane displacements $u_z(x, y, H)$ of the thin plate. A triple point noted Y is observed on the morphological map on which may coexist the three buckling structures. An ~~unexpected~~ intermediate domain (referred to as (I) in the following) is also observed all along the (B) domain in Fig. 2a. It corresponds to a transition domain between the bubbles and either the telephone cord or the straight-sided buckles. The (I) domain is dissociated into two sub-areas, the upper one (transition mainly from (B) to (TC), labelled (I^+)) where buckles are characterized by a kind of hook-like structures, and the lower one (transition from (B) to (SSB) referred to as domain (I^-)) where buckles are characterized by bone-like structures (see Fig. 2b).

FEM morphological maps have been extracted for seven α values, namely α=-0.999 (assumed as the case of a hard substrate α=-1), α=0, α=0.5, α=0.75, α=0.9, α=0.95 and α=0.99. Only some of this data is reported in Fig. 3, for clarity. It is shown first that the (SSB) domain boundary does not significantly evolve with α (Fig. 3a). It is well-known that the SSB exhibits a nanometer scale depression on both sides, which deepens as α is increased [26,27]. Although the equilibrium SSB shape is thus modified, the stability (SSB) domain is seen to be unaffected by the substrate elasticity. Secondly, the intermediate domain (I) is observed for any value of α and is seen to shift up on the map for high β values, as α is increased. Finally, the

triple point Y is clearly shifted towards lower (β_t;β_l) coordinates with the increase of α (see Fig. 3b for a zoom of Fig. 3a). All these results suggest that the soft character of the substrate promotes the telephone cords by enlarging its domain of mechanical stability.

In order to quantify the substrate elasticity effect, the (TC) domain size has been characterized in the following by its width $\Delta\beta_l^{TC}$ defined as the distance between the upper and lower limits of the (TC) domain in the diagram, along the β_l axis. The evolution of $\Delta\beta_l^{TC}$ is presented in Fig. 4 as a function of α, for various β_t values. It is shown that $\Delta\beta_l^{TC}$ is approximately constant up to α=0.5 above which a first slight increase is observed followed by a huge one for α>0.8. It is noted that this behavior is similar to what has been observed both for the maximum deflection of a SSB and for the critical stress for buckling to occur [26,27]. In addition, for a given α value, the enlargement of the (TC) domain continuously increases with the increasing β_t. To fix the idea, let us consider a metallic film ($\bar{E}_f$ = 200 GPa) of thickness h=200 nm, a buckle of width $2b$=10 µm and an internal stress σ=2.2 GPa (related to β_t=28) usually obtained experimentally in thin films [1]. For α=-1, it leads to $\Delta\sigma_l^{TC}=0.08\Delta\beta_l^{TC}$=0.4 GPa = ±200 MPa; for α=0.95, $\Delta\sigma_l^{TC}\approx$1.4 GPa = ± 700 MPa. Due to the high elastic contrast between the film and the substrate, the width of the (TC) domain is consequently enlarged by a factor 3.5 at a stress of 2.2 GPa, from [2.0-2.4] to [1.5-2.9].

In the following, the triple equilibrium point Y is defined by its coordinates (Y_t;Y_l) on the morphological map. The evolution of Y_t and Y_l are presented in Fig. 5, as a function of α. The error bars on the graph correspond to uncertainties on the Y position manually determined on each α value map. A significant decrease of both Y_t and Y_l with increasing α values is clearly observed. The decrease is however more pronounced in the case of Y_t. When normalized over the value obtained for a hard substrate [24] ($Y_t^{\alpha=-1}$=20.31 and $Y_l^{\alpha=-1}$=21.61), it leads for α=0.95 to a huge decrease of approximately 40% for Y_t and 23% for Y_l. Similarly to $\Delta\beta_l^{TC}$, the

dependence of Y with α consequently contributes to enlarge the stability domain of TC-type buckling structures.

Similarly to the (TC) domain, $\Delta\beta_l^I$ is defined as the width of the (I) domain along the longitudinal axis. The evolution of $\Delta\beta_l^I$ is presented in Fig. 6 as a function of α, for various β_t values. As observed for the (TC) domain, $\Delta\beta_l^I$ continuously increases with the increase of α, a huge increase being observed for $\alpha>0.8$. The effect of the substrate elasticity is consequently both to enlarge and to shift up the intermediate (I) domain to higher stresses. The (I) domain is quite narrow in β units, which may explain why the associated buckling structures were rarely discussed in the literature. Such a transition domain was however experimentally evidenced on strained polycarbonate plates [32]. What the authors in [32] called 'oblique bumps' were explained as a resonant combination of the symmetric and anti-symmetric modes of the bubbles and the telephone cords. These structures may reasonably correspond to the hook-like buckles in (I^+). Additionally, the evolution of a nickel 50 nm thick film deposited on a polycarbonate substrate under two different mechanical loadings is presented in Fig. 7. The coated specimen, for which α is experimentally equal to 0.95, was first strained by compression of the substrate under the (O*y*) axis. As expected [24,27-30], SSBs are generated at the sample surface, lying perpendicularly to the compression axis. At the maximum external loading, the film is thus submitted to an anisotropic stress with $\sigma_{yy}>\sigma_{xx}$; one characteristic straight-sided buckle is shown in Fig. 7a. The external applied stress was then released, so that the film was only submitted to the internal isotropic stress ($\sigma_{yy}=\sigma_{xx}$); it results in the morphological evolution of the SSB, as observed in Fig. 7b. As for the TC to SSB evolution [24], no further transversal delamination was observed once the delaminated stripe was created, even after mechanical cycles. The width 2*b* does not evolve anymore due to the value of the mode mixity ψ parameter measuring the mode II to mode I loading ratio at the interface [9,27,28]. The resulting buckled structure is

neither a SSB, nor a line of bubbles, and is in good agreement with the bone-like buckle evidenced numerically in the domain (I^-) (see Fig. 2b). Taking the experimental values of h=50 nm, $\bar{E}_f$=180 GPa, $2b$=3 μm and for α=+0.95, the width of the (I) domain in stress unit was estimated from Fig. 6 to be $\Delta\sigma_l^I=0.05\Delta\beta_l^I$= 0.6 GPa=±300 MPa at a stress of 1.4 GPa (β_t=28). For a higher stress, $\Delta\sigma_l^I$ is strongly increased; for instance at a stress of 2 GPa (β_t=40), it goes up to $\Delta\sigma_l^I$=2.4 GPa=±1.2 GPa. This huge enlargement of the (I) domain may explain why we succeed to experimentally observe such an intermediate buckle shown in Fig. 7.

In conclusion, we have studied the effect of substrate elasticity on the equilibrium shapes of buckling structures by means of finite elements methods simulations. The elastic mismatch between the film and the substrate was characterized by its Dundurs' coefficient α. First, a transition domain is evidenced between the bubbles and either the straight-sided or the telephone cord buckles, irrespective of the substrate elasticity. In addition, it is shown that the straight-sided buckle domain does not significantly evolve with the increase of α, while the equilibrium domain of the common telephone cords is strongly enlarged. It demonstrates that a high elastic contrast between the film and the substrate allows for telephone cords to be energetically favorable for even lower stresses. It consequently suggests that the plane state stability domain of the film is smaller in size in the case of film/substrate systems exhibiting a high elastic contrast. It is believed that our results will give new insight on how to limit, or even prevent, the occurrence of buckling structures, of importance for the development of flexible devices.

4. Appendix

Details of the finite element modeling parameters are provided in this part. The film is modeled by two-dimensional, triangular shell elements of type (S3R) from the ABAQUS library, including a finite membrane strain formulation, and arbitrarily large rotations with linear interpolation degrees of freedom and reduced integration. The substrate is meshed with four-node tetrahedral solid elements of type (C3D4) with linear interpolation degrees of freedom. The mesh used for the simulation box is displayed in Fig. 8a. Areas with different mesh densities were used, the mesh being finer near the borders of the delaminated stripe, and becomes coarser when moving away from those borders. The degree of mesh refinement is quantified in Fig. 8b with respect to the delaminated stripe width $2b$. It can be seen that, if the elements characteristic size is $2b/20$ in most of the stripe, this size drops to $2b/400$ at the stripe boundary, with a transition zone from coarser to finer meshes. This mesh distribution helps capturing more accurately the solution in the region where soft substrates are submitted to particularly high strains. Additionally, in order to check that the mesh density is high enough, calculations were carried out with dividing each one of these characteristics sizes by a factor two. Load versus displacement curves were plotted and no differences were observed. The equilibrium shapes were not modified either.

Acknowledgements

This work pertains to the French government program ”Investissements d’Avenir” (LABEX INTERACTIFS, ANR-11-LABX-0017-01). Y. Ni was supported by the Strategic Priority Research Program of the Chinese Academy of Sciences (Grant No. XDB22040502).

Figures caption

Figure 1: Simulation box used for the finite element calculations, with the film modeled as a plate on a substrate represented as a 3D parallelepiped. The delaminated area is a rectangular stripe of width 2*b*, delimited by dashed lines, where buckling patterns may develop.

Figure 2: (a) Map of buckle morphologies as a function of normalized transversal β_t and longitudinal (main buckle axis) β_l stresses, for α=0. The isotropic stresses for which β_t=β_l has been superimposed as a straight green line on the graph. (SSB), (B), (TC) and (I) domains correspond to the equilibrium of straight-sided buckles, bubbles, telephone cords and intermediate buckles, respectively. The (I) domain shaded in grey is divided in an upper (I^+) and (lower I^-) subdomains. The characteristic buckling structures for α=0 are presented in (b) by their out-of-plane displacements, for SSB (β_t=24.37; β_l=21.12), for B (β_t=20.31; β_l=27.78), for TC (β_t=40.62; β_l=45.98), for I^+ (β_t=36.56; β_l=46.06,) and for I^- (β_t=16.25; β_l=19.50).

Figure 3: Map of buckle morphologies as a function of normalized transversal β_t and longitudinal β_l stresses, for various α values. (SSB), (B), (TC) and (I) domains correspond to straight-sided buckles, bubbles, telephone cords and intermediate buckles, respectively. (a) large overview (b) zoom around the triple point Y.

Figure 4: Width of the (TC) domain along the longitudinal direction $\Delta\beta_l^{TC}$ *vs*. Dundurs' coefficient α for various β_t values.

Figure 5: Transversal Y_t and longitudinal Y_l coordinates (in β_t and β_l units) of the triple point Y, as a function of Dundurs' coefficient α.

Figure 6: Width of the (I) domain along the longitudinal direction $\Delta\beta_l^I$ *vs*. Dundurs' coefficient α for various β_t values.

Figure 7: Buckled structures investigated by atomic force microscopy on a nickel 50 nm thick film deposited by physical vapor deposition on a polycarbonate substrate, for (a) an anisotropic external loading $\sigma_{yy}>\sigma_{xx}$ induced by a unilateral compression of the substrate along the longitudinal (O*y*) axis (b) an isotropic internal loading $\sigma_{yy}=\sigma_{xx}$.

Figure 8: Detail of the FEM meshing. (a) Global view of the system mesh (b) Details of the mesh density, with element sizes expressed as fractions of the delaminated stripe width 2*b*.

References

[1] G. Abadias, E. Chason, J. Keckes, M. Sebastiani, G.B. Thompson, E. Barthel, G.L. Doll, C.E. Murray, C.H. Stoessel and L. Martinu, Review Article: Stress in thin films and coatings: Current status, challenges, and prospects, J. Vac. Sci. Technol. A 36 (2018) 020801, 10.1116/1.5011790.

[2] J. Tranchant, B. Angleraud, X. L. Han, J. P. Landesman and P. Y. Tessier, Carbon nanochannels elaborated by buckle delamination control on patterned substrates, Appl. Phys. Lett. 91 (2007) 013103, 10.1063/1.2753536.

[3] H. Ren, Z. Xiong, E. Wang, Z. Yuan, Y. Sun, K. Zhu, B. Wang, X. Wang, H. Ding, P. Liu, L. Zhang, J. Wu, S. Fan, X. Li, and K. Liu, Watching Dynamic Self-Assembly of Web Buckles in Strained MoS2 Thin Films, ACS Nano 13 (2019) 3106-3116, 10.1021/acsnano.8b08411.

[4] S. J. Kim, D.W. Kim, J. Lim, S. Y. Cho, S. O. Kim, H. T. Jung, Large-Area Buckled MoS2 Films on the Graphene Substrate, ACS Appl. Mater. Inter. 8 (2016) 13512-13519, 10.1021/acsami.6b01828.

[5] Z. Zhen, Z. Li, X. Zhao, Y. Zhong, L. Zhang, Q. Chen, T. Yang, and H. Zhu, Formation of Uniform Water Microdroplets on Wrinkled Graphene for Ultrafast Humidity Sensing, Small 14 (2018) 1703848, 10.1002/smll.201703848.

[6] F. Zou, H. Zhou, D. Y. Jeong, J. Kwon, S. U. Eom, T. J. Park, S. W. Hong and J. Lee, Wrinkled Surface-Mediated Antibacterial Activity of Graphene Oxide Nanosheets, ACS Appl. Mater. Inter. 9 (2017) 1343-1351, 10.1021/acsami.6b15085.

[7] Y. Liu, K. Y. Guo ,S.Sonam, S. K. Hong, M. H. Nai, C. T. Nai, L. Gao, J. Chen, B. J. Cho, C. T. Lim, W. Guo and K. P. Loh, Large-Area, Periodic, Hexagonal Wrinkles on Nanocrystalline Graphitic Film, Adv. Funct. Mater. 25 (2015) 5492-5503, 10.1002/adfm.201502010.

[8] R. Boijoux, G. Parry, C. Coupeau, Buckle depression as a signature of Young's modulus mismatch between a film and its substrate, Thin Solid Films 645 (2018) 379-382. 10.1016/j.tsf.2017.11.011.

[9] J. Hutchinson, Z. Suo, Mixed mode cracking in layered materials, Adv. Appl. Mech., Elsevier, 1991, pp. 63–191.

[10] M. W. Moon, H. M. Jensen, J. W. Hutchinson, K. H. Oh and A. G. Evans, The characterization of telephone cord buckling of compressed thin films on substrates, J. Mech. Phys. Solids 50 (2002) 2355-2377, 10.1016/S0022-5096(02)00034-0.

[11] M. J. Cordill, D. F. Bahr, N. R. Moody, and W. W. Gerberich, Adhesion measurements using telephone cord buckles, Mater. Sci. Eng. A-Struct. 443 (2007) 150-155, 10.1016/j.msea.2006.08.027.

[12] K. Pan, Y. Ni, and L. He, Effects of interface sliding on the formation of telephone cord buckles, Phys. Rev. E 88 (2013) 062405, 10.1103/PhysRevE.88.062405.

[13] S. J. Yu, X. Xiao, M. Chen, H. Zhou, J. Chen, P. Si, Z. Jiao,
Morphological selections and dynamical evolutions of buckling patterns in SiAlNx films: From straight-sided to telephone cord or bubble structures, Acta Mater. 64 (2014) 41-53, 10.1016/j.actamat.2013.11.038

[14] J.-Y. Faou, G. Parry, S. Grachev, and E. Barthel, Telephone cord buckles-A relation between wavelength and adhesion, J. Mech. Phys. Solids 75 (2015) 93-103, 10.1016/j.jmps.2014.11.008.

[15] J.-Y. Faou, S. Grachev, E. Barthel, G. Parry, From telephone cords to branched buckles: A phase diagram, Acta Mater. 125 (2017) 524-531, 10.1016/j.actamat.2016.12.025.

[16] M. W. Moon, K.R. Lee, K. Oh, J. Hutchinson, Buckle delamination on patterned substrates, Acta Mater. 52 (2004) 3151-3159, 10.1016/j.actamat.2004.03.014.

[17] S. J. Yu, L. Ma, J. Zhang, L. He, Y. Ni, Localization of wrinkle patterns by crack-tip induced plasticity: Experiments and simulations, Int. J. Solids Struct. 178 (2019) 108-119, 10.1016/j.ijsolstr.2019.06.004.

[18] M. J. Cordill, N.R. Moody, D.F. Bahr, The effects of plasticity on adhesion of hard films on ductile interlayers, Acta Mater. 53 (2005) 2555-2562, 10.1016/j.actamat.2005.02.013.

[19] K. Pan, Y. Ni, L. He, R. Huang, Nonlinear analysis of compressed elastic thin films on elastic substrates: From wrinkling to buckle-delamination, Int. J. Solids Struct. 51 (2014) 3715-3726, 10.1016/j.ijsolstr.2014.07.005.

[20] Y. Ni, S. Yu, H. Jiang, L. He, The shape of telephone cord blisters, Nat. Commun. 8 (2017) 14138, 10.1038/ncomms14138.

[21] A. Kleinbichler, M.J . Pfeifenberger, J. Zechner, S. Wöhlert, M.J.Cordill, Scratch induced thin film buckling for quantitative adhesion measurements, Materials & Design 155 (2018) 203-211, 10.1016/j.matdes.2018.05.062

[22] L. Marot, G. De Temmerman, M.A. van den Berg, P.O. Renault, G. Covarel, M. Joanny, J.M. Travère, R. Steiner, D. Mathys, E. Meyer, ITER first mirror mock-ups exposed in Magnum-PSI, Nucl. Fusion 56 (2016) 066015, 10.1088/0029-5515/56/6/066015

[23] B. Eren, L. Marot, G. Gunzburger, P.O. Renault, Th. Glatzel, R. Steiner, E. Meyer, Hydrogen-induced buckling of gold films, J. Phys. D: Appl. Phys. 47 (2014) 025302, 10.1088/0022-3727/47/2/025302

[24] G. Parry, A. Cimetière, C. Coupeau, J. Colin, J. Grilhé, Stability diagram of unilateral buckling patterns of strip-delaminated films, Phys. Rev. E 74 (2006) 066601, 10.1103/PhysRevE.74.066601.

[25] H. H. Yu and J. W. Hutchinson, Influence of substrate compliance on buckling delamination of thin films, Int. J. Fracture 113 (2002) 39-55, 10.1023/A:1013790232359.

[26] G. Parry, J. Colin, C. Coupeau, F. Foucher, A. Cimetière, J. Grilhé, Effect of substrate compliance on the global unilateral post-buckling of coatings: AFM observations and finite element calculations, Acta Mater. 53 (2005) 441-447, 10.1016/j.actamat.2004.09.039.

[27] R. Boijoux, G. Parry, J. Y. Faou, C. Coupeau, How soft substrates affect the buckling delamination of thin films through crack front sink-in, Appl. Phys. Lett. 110 (2017) 141602, 10.1063/1.4979614.

[28] C. Coupeau, R. Boijoux, Y. Ni, G. Parry, Interacting straight-sided buckles: An enhanced attraction by substrate elasticity, J. Mech. Phys. Solids 124 (2019) 526-535, 10.1016/j.jmps.2018.11.010.

[29] F. Cleymand, C. Coupeau, J. Grilhé, Experimental investigation of the instability of buckling patterns: From straight-sided to wormlike structures, Scripta Mat. 44 (2001) 2623-2627, 10.1016/S1359-6462(01)00969-1.

[30] F. Cleymand, C. Coupeau, J. Grilhé, Atomic force microscopy investigation of buckling patterns of nickel thin films on polycarbonate substrates, Phil. Mag. Lett. 82 (2002) 477-482, 10.1080/09500830210154688.

~~[31] N. Vu-Bac, T.X. Duong, T. Lahmer, X. Zhuang, R.A. Sauer, H.S. Park, T. Rabczuk, A NURBS-based inverse analysis for reconstruction of nonlinear deformations of thin shell structures, Comput. Methods Appl. Mech. Eng. 331 (2018) 427-455, 10.1016/j.cma.2017.09.034.~~

~~[32] N. Vu-Bac, T.X. Duong, T. Lahmer, P. Areias, R.A. Sauer, H.S. Park, T. Rabczuk, A NURBS-based inverse analysis of thermal expansion induced morphing of thin shells, Comput. Methods Appl. Mech. Eng. 350 (2019) 480-510, 10.1016/j.cma.2019.03.011.~~

[31] Abaqus Manuals Collection, Dassault Systems; Simulia Corp., Providence, RI, USA, 2013.

[32] B. Audoly, B. Roman, and A. Pocheau, Secondary buckling patterns of a thin plate under in-plane compression, Eur. Phys. J. B 27 (2002) 7-10, 10.1140/epjb/e20020124.

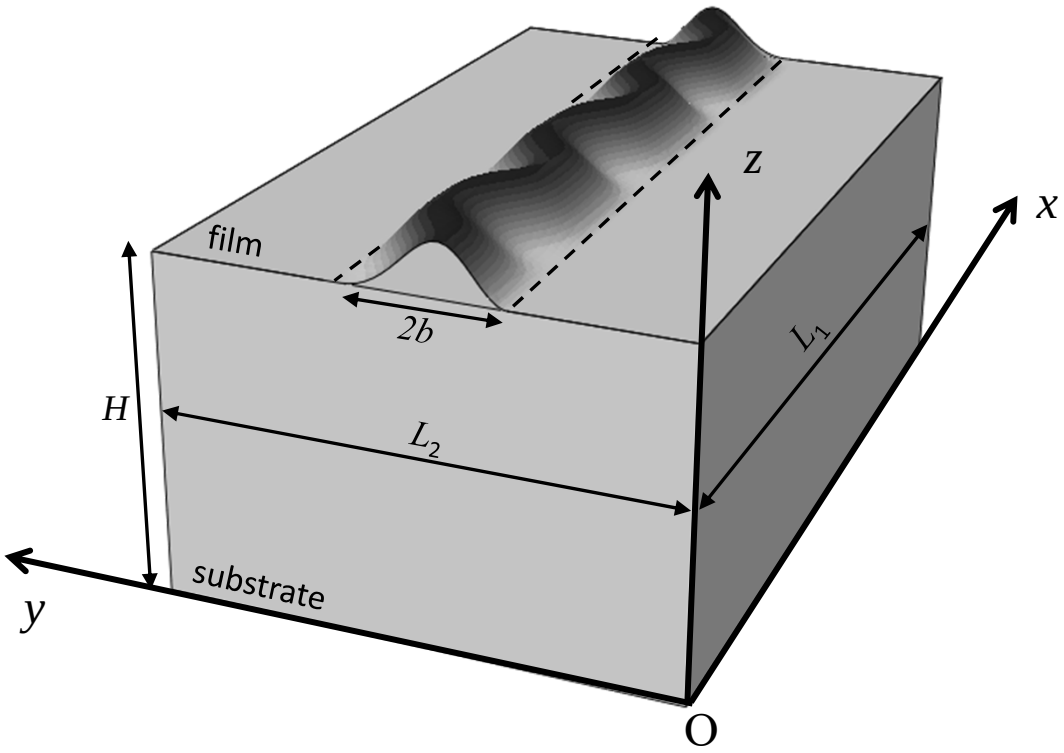

Figure 1

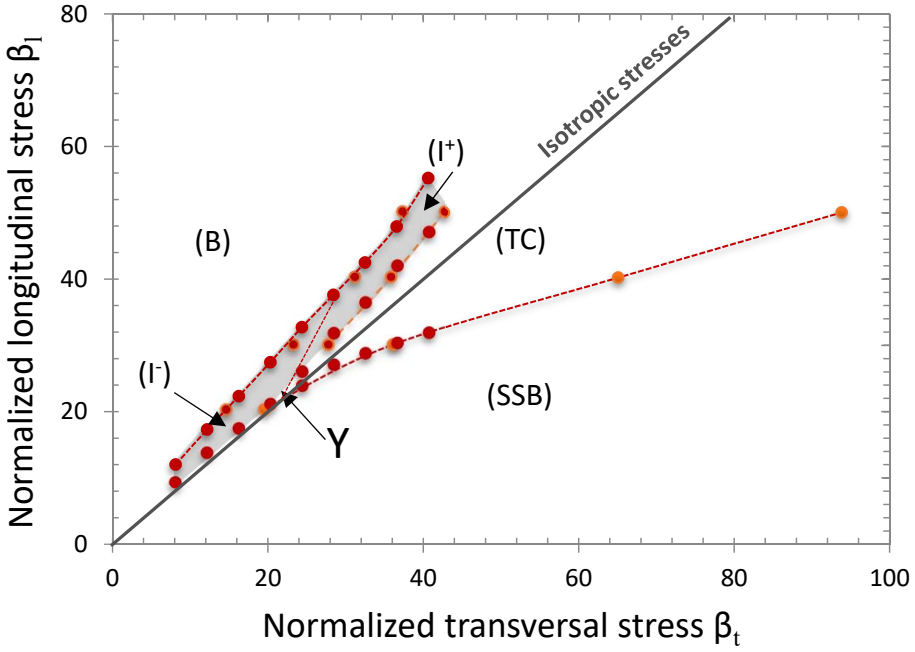
Normalized longitudinal stress β_l
Normalized transversal stress β_t
0
20
40
60
80
100
Isotropic stresses
(I+)
(I-)
(B)
(TC)
(SSB)
Y

(a)

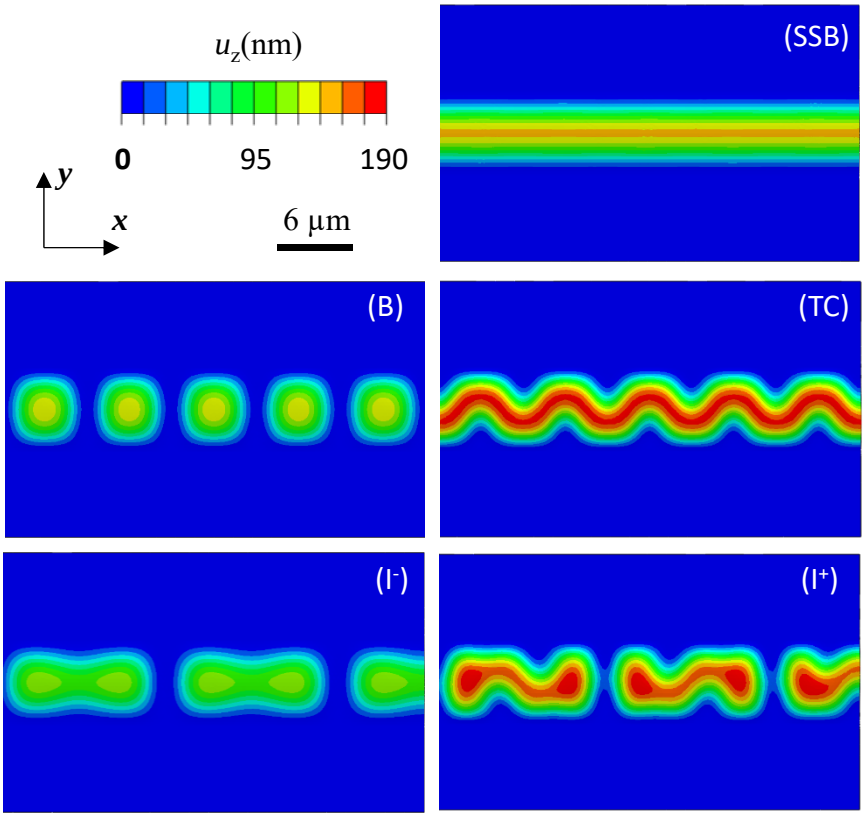
u_z(nm)
0
95
190
y
x
6 µm
(SSB)
(B)
(TC)
(I-)
(I+)

(b)

Figure 2

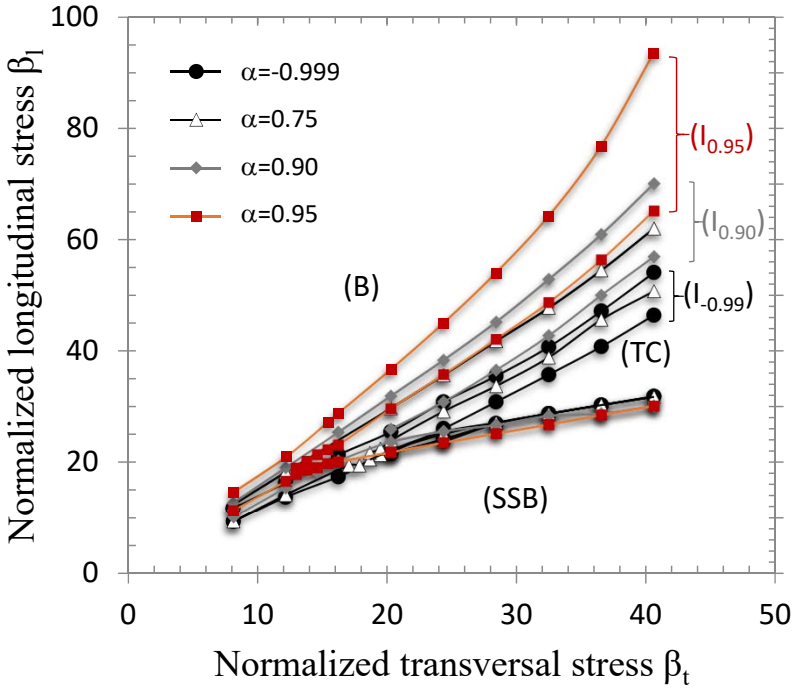
Normalized longitudinal stress β_l
Normalized transversal stress β_t
α=-0.999
α=0.75
α=0.90
α=0.95
(B)
(TC)
(SSB)
$(I_{0.95})$
$(I_{0.90})$
$(I_{-0.99})$
0
20
40
60
80
100
0
10
20
30
40
50

(a)

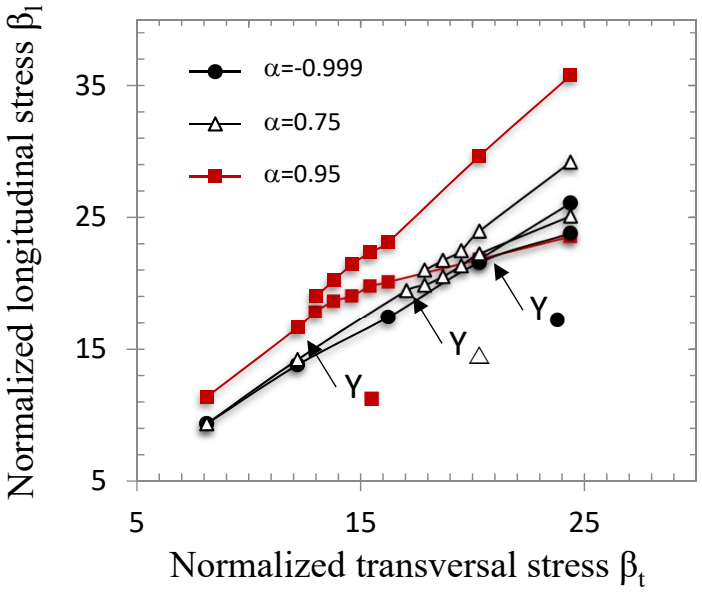
Normalized longitudinal stress β_l
Normalized transversal stress β_t
α=-0.999
α=0.75
α=0.95
$Y_{\bullet}$
$Y_{\triangle}$
$Y_{\blacksquare}$
5
15
25
35
5
15
25

(b)

Figure 3

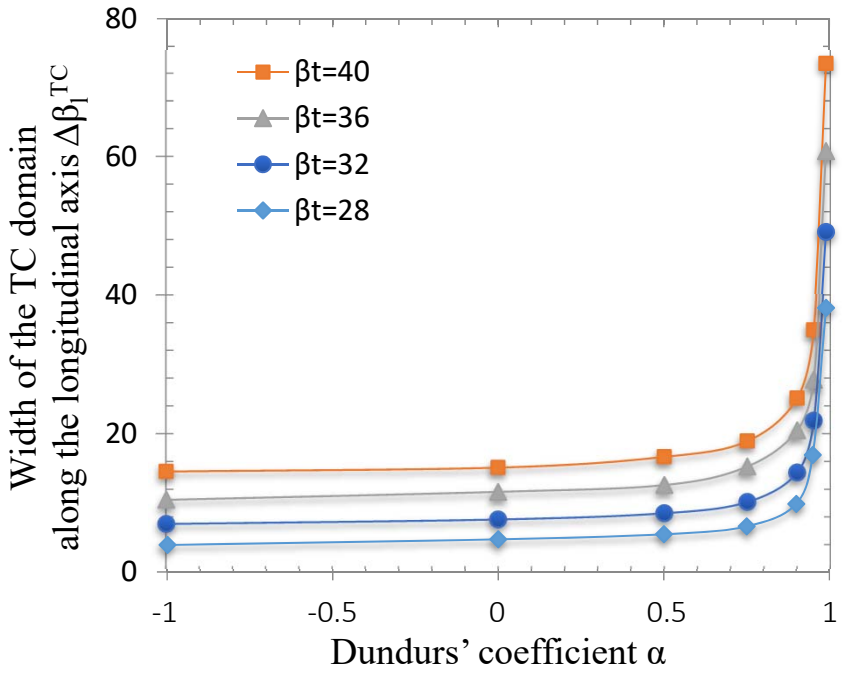
80
60
40
20
0
-1
-0.5
0
0.5
1
βt=40
βt=36
βt=32
βt=28
Width of the TC domain
along the longitudinal axis $\Delta\beta_l^{TC}$
Dundurs' coefficient α

Figure 4

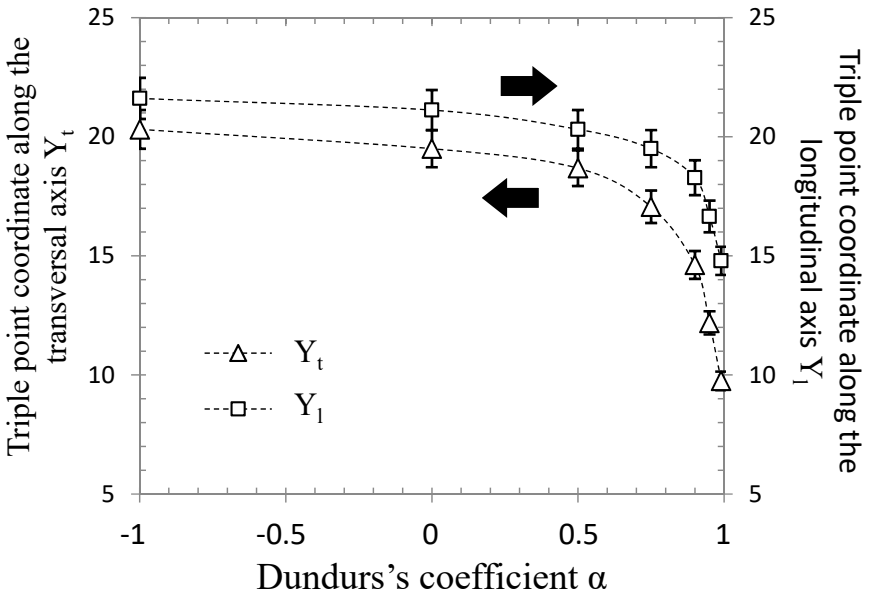
Triple point coordinate along the transversal axis Y_t
Triple point coordinate along the longitudinal axis Y_l
Dundurs's coefficient α
Y_t
Y_l
25
20
15
10
5
-1
-0.5
0
0.5
1

Figure 5

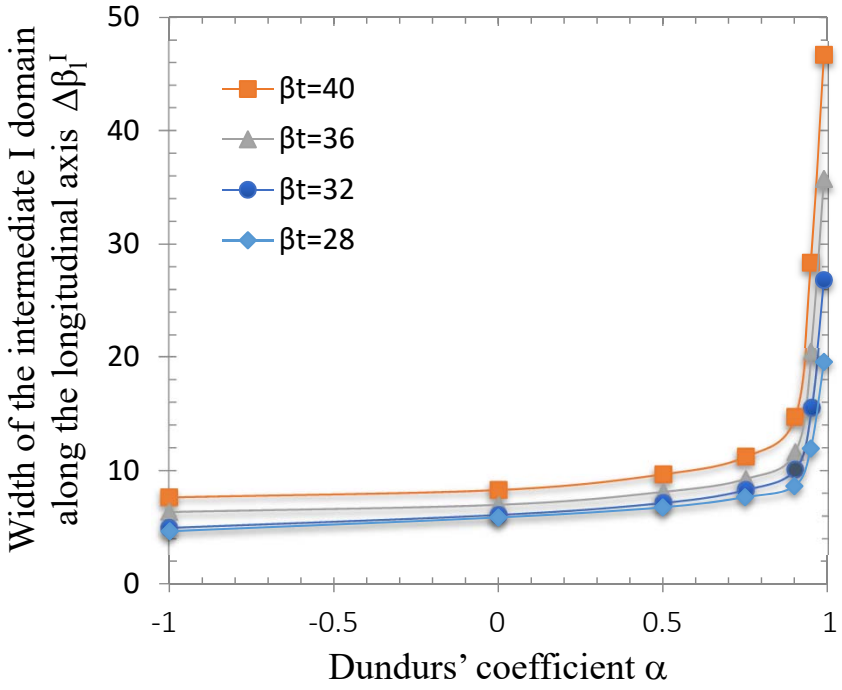
Width of the intermediate I domain along the longitudinal axis $\Delta\beta_I^I$
50
40
30
20
10
0
βt=40
βt=36
βt=32
βt=28
-1
-0.5
0
0.5
1
Dundurs' coefficient α

Figure 6

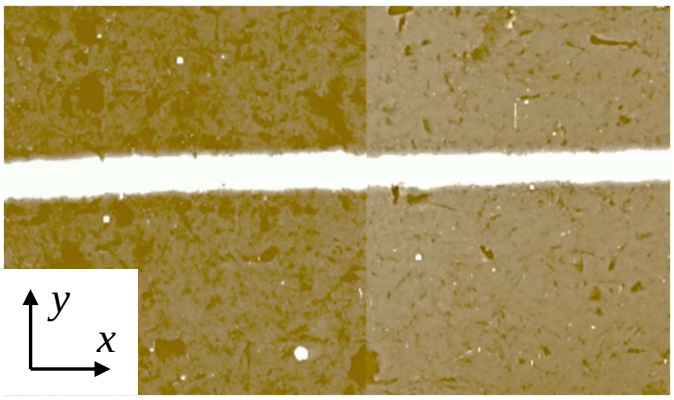

(a)

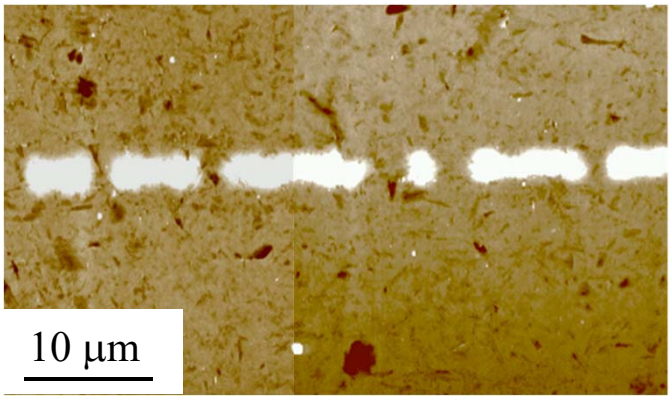

(b)

Figure 7

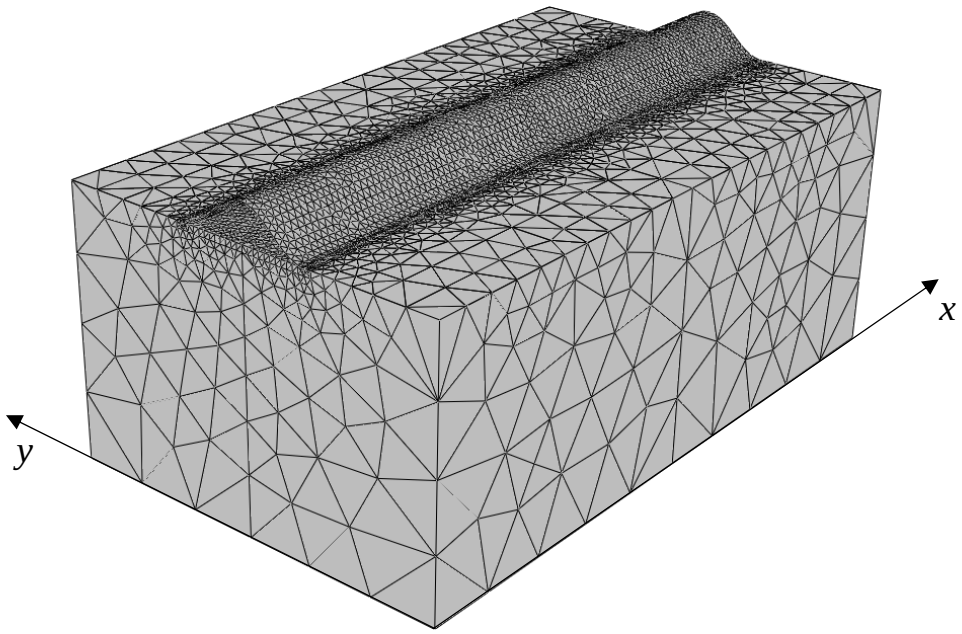

(a)

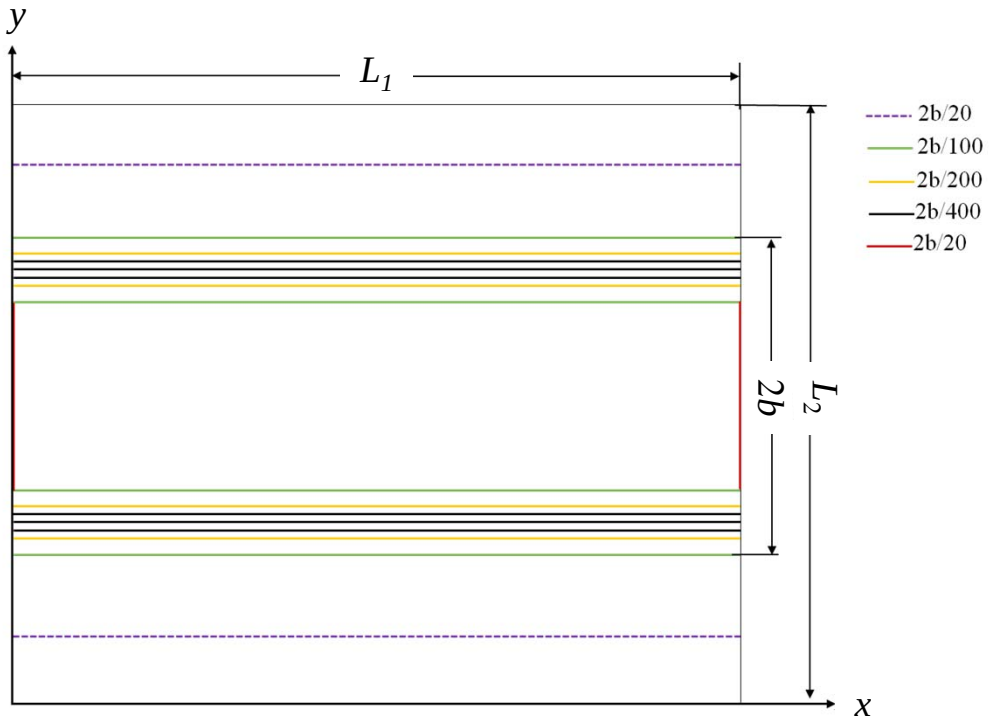

(b)

Figure 8

TABLE

Film thickness h (nm)	Substrate thickness H (µm)	Longitudinal size of the FEM cell L_1 (µm)	Lateral size of the FEM cell L_2 (µm)
50	12 (100 for $\alpha \geq 0.95$)	30	18 (54 for $\alpha \geq 0.95$)
Young's modulus of the film E_f (GPa)	Poisson ratio of the film ν_f	Poisson ratio of the substrate ν_s	Width of the delaminated stripe $2b$ (µm)
160	0.31	0.34	6

Table 1 : Summary of the parameters used for the FEM modeling